Science Advances

AAAS

advances.sciencemag.org/cgi/content/full/3/5/e1602522/DC1

Supplementary Materials for

Dynamic and programmable self-assembly of micro-rafts at the air-water interface

Wendong Wang, Joshua Giltinan, Svetlana Zakharchenko, Metin Sitti

Published 24 May 2017, *Sci. Adv.* **3**, e1602522 (2017)
DOI: 10.1126/sciadv.1602522

The PDF file includes:

Other Supplementary Material for this manuscript includes the following:
(available at advances.sciencemag.org/cgi/content/full/3/5/e1602522/DC1)

- movie S4 (.mp4 format). The assembly of three free micro-rafts with an arc angle of 30°.
- movie S5 (.mp4 format). The assembly of one free and two attached micro-rafts with an arc angle of 30°.
- movie S6 (.mp4 format). The assembly of four free micro-rafts with an arc angle of 30°.
- movie S7 (.mp4 format). The assembly of one free and three attached micro-rafts with an arc angle of 30°.
- movie S8 (.mp4 format). The assembly of four free micro-rafts with an arc angle of 90°.
- movie S9 (.mp4 format). The disassembly of four assembled micro-rafts with an arc angle of 90°.
- movie S10 (.mp4 format). The rearrangement of four assembled micro-rafts with an arc angle of 90° into a diamond shape.
- movie S11 (.mp4 format). The rearrangement of four assembled micro-rafts with an arc angle of 90° into a square shape.
- movie S12 (.mp4 format). The assembly of 40 micro-rafts with an arc angle of 30°.
- movie S13 (.mp4 format). The assembly of 40 micro-rafts with an arc angle of 90°.
- movie S14 (.mp4 format). The local rearrangement of assembled structures of 40 micro-rafts with an arc angle of 30° at intermediate spinning speed.

table S1. Contact angles of noncoated and SAM-coated gold surface.

Sample	Advancing Contact Angle (°)	Receding Contact Angle (°)
Au surface (Day 1)	45±9	18±3
Au surface (Day 2)	63±5	20±3
Au surface (Day 5)	85±5	17±5
1-heptanethiol SAM – Au Surface	96±2	50±2

Note: The receding contact angles of the bare Au surface are very difficult to measure accurately, so we chose the angle when the droplet volumes were the smallest. However, it is likely that the receding contact angle is close to zero. Contact angles were measured on Krüss DSA 100.

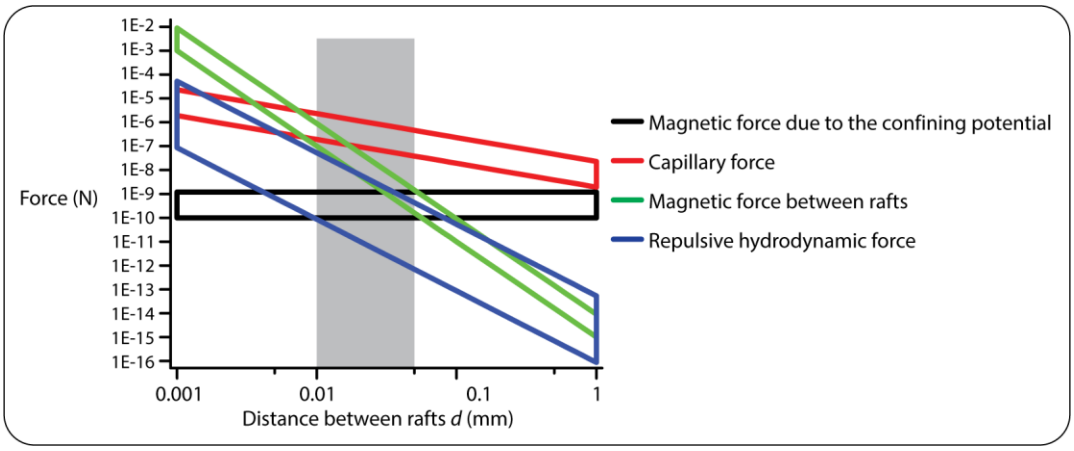

fig. S1. Scaling analysis of various forces in the system. The gray area corresponds to the region where our experiments lie.

Note 1: Equations used in the scaling analysis in fig. S1:

Magnetic attractive force due to the overall confining potential: $F_m = O(m \cdot \nabla B)$

Capillary force: $F_c = O(\gamma \cdot A \cdot R\theta/d)$

Magnetic attractive force due to dipole-dipole interaction between micro-rafts: $F_{d-d} = O(\frac{\mu_0}{4\pi} \cdot \frac{m^2}{d^4})$

Repulsive hydrodynamic force: $F_h = O(\rho\omega^2 R^7/d^3)$

Note 2: Values used:

Magnetic moment of one micro-raft (obtained from fig. S2): $m = 1\sim3 \times 10^{-10} A \cdot m^2$

Gradient of the overall magnetic potential (obtained from fig. S3): $\nabla B = 1\sim4\, T/m$

Surface tension of water: $\gamma = 74\ mN/m$

Amplitude: $A = 1{\sim}4\ \mu m$

Radius of the micro-raft: $R = 50\ \mu m$

Arc angle of the cosinusoidal profile: $\theta = \frac{\pi}{6} \sim \frac{\pi}{2}$

Density of water: $\rho = 1000\ kg/m^3$

Spinning speed: $\omega = 100 \sim 2500\ rpm = 10.5 \sim 261\ rad/s$

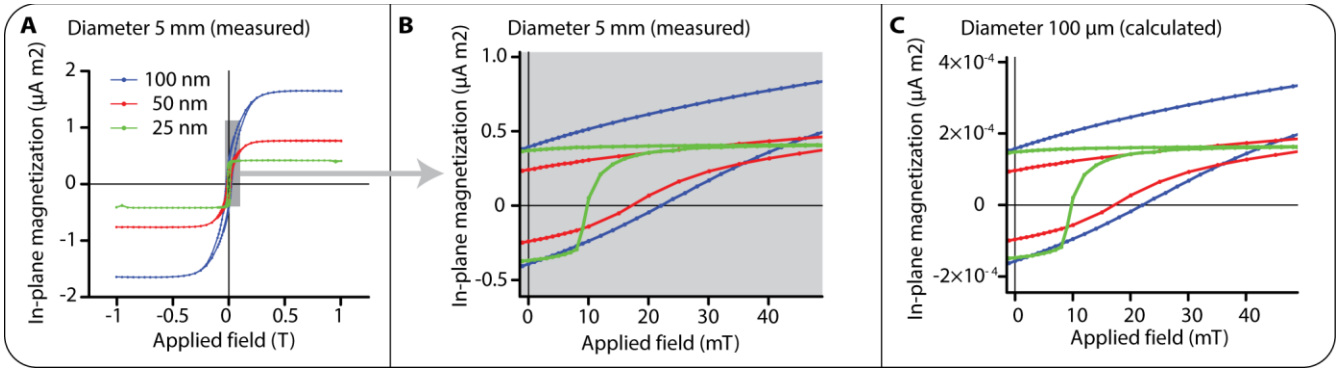

fig. S2. In-plane magnetization of cobalt thin films. Cobalt thin films of various thickness were sputtered on a clean cover slip (#1.5); a further 30 nm thick gold layer was also sputtered. Then they were cut into circles of 5mm diameter on LPKF ProtoLaser U3 before measurement on MPMS-XL (Magnetic Property Measurement System) Magnetometer by Quantum Design based on a SQUID (Superconducting Quantum Interference Device). (**A**, **B**) measured hysteresis curves at different zooms. (**C**) Calculated data of the magnetic moment of a disk of diameter 100 µm, which we use to estimate the magnetic moment of one individual micro-raft. The result is used in the scaling analysis in fig. S1.

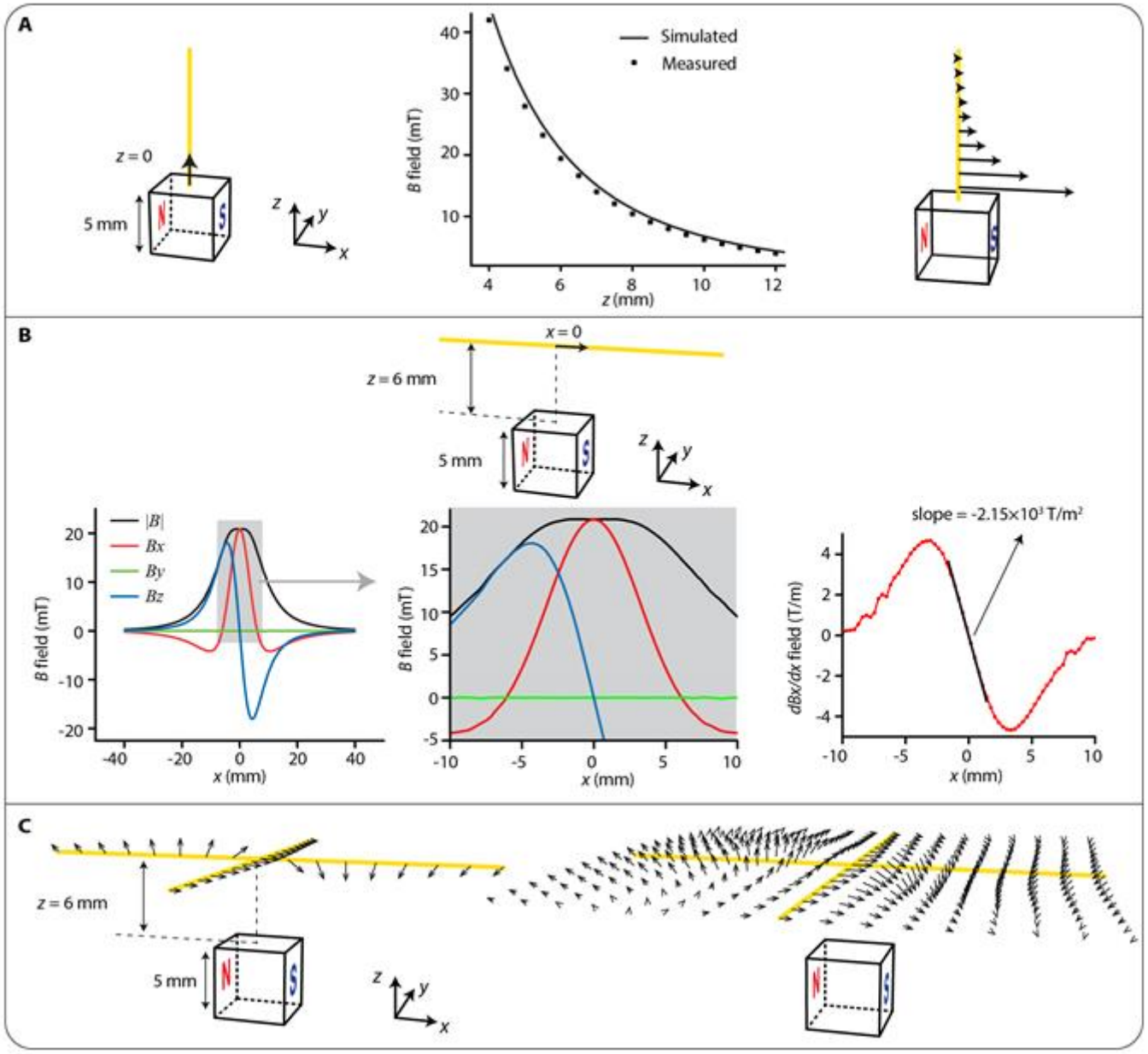

fig. S3. Magnetic profile of a 5-mm cube magnet. (**A**) Magnetic field along the *z*-direction. The measured data match well with the simulated curve. (**B**) Magnetic field along the *x*-direction at *z* = 6mm above the top surface of the magnet. The z = 6mm is the height at which all the experiments were conducted. The gradient of the magnetic field is used in the scaling analysis in fig. S1. The slope calculated in the plot dB_x/dx vs. x is used in the simulation. The region within a radius of ~2 mm from center is larger than the largest size of dynamic assembly, which is ~0.5 mm in radius. The relation dB_x/dx ~ r is therefore justified in the simulation. (**C**) An overview of the magnetic field at *z* = 6mm in both *x* and *y* directions.

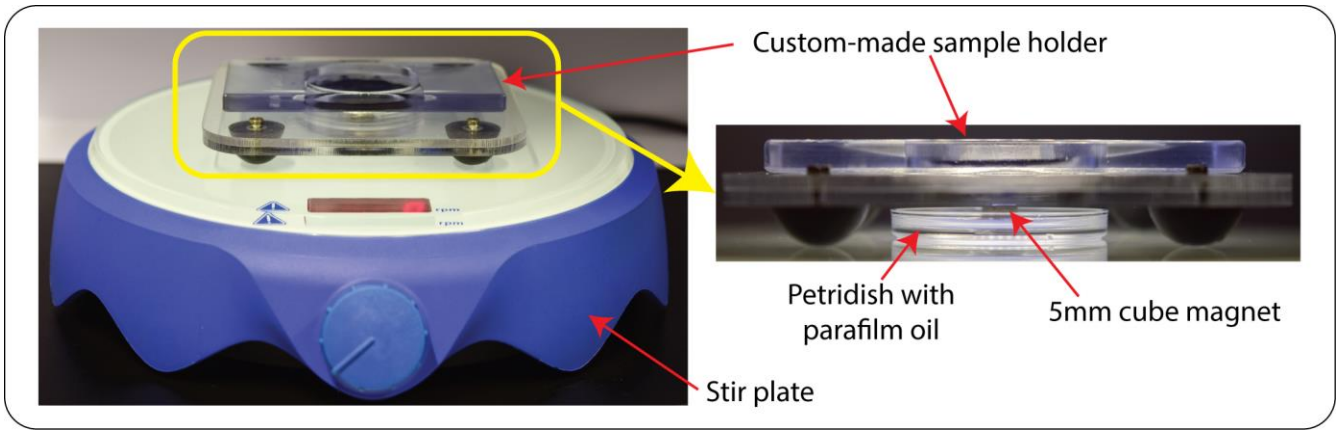

fig. S4. Photos of the experimental setup. The custom-made sample holder consists of two parts: The bottom part has four rubber semi-spherical feet (color black) that damp vibration that may transmit from the bottom stir plate to the top part of the sample holder, and the top sample is 3D-printed.

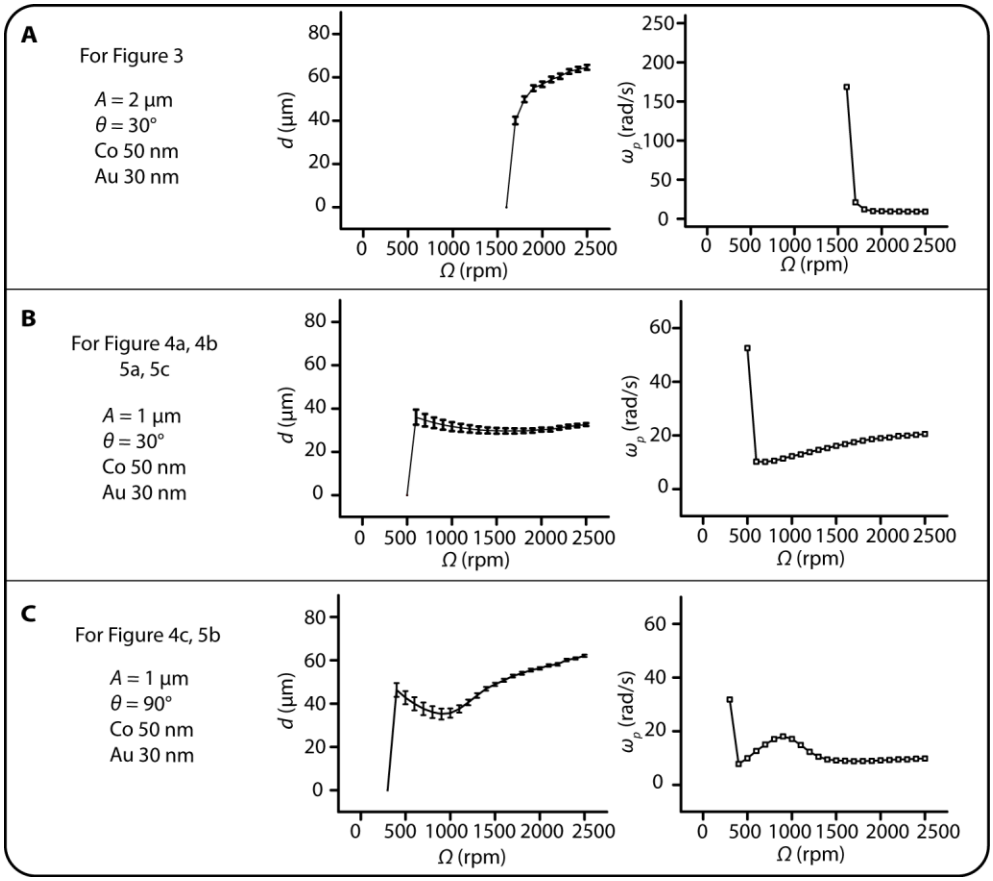

fig. S5. Pairwise interaction plots for micro-rafts used in Figs. 3 to 5.

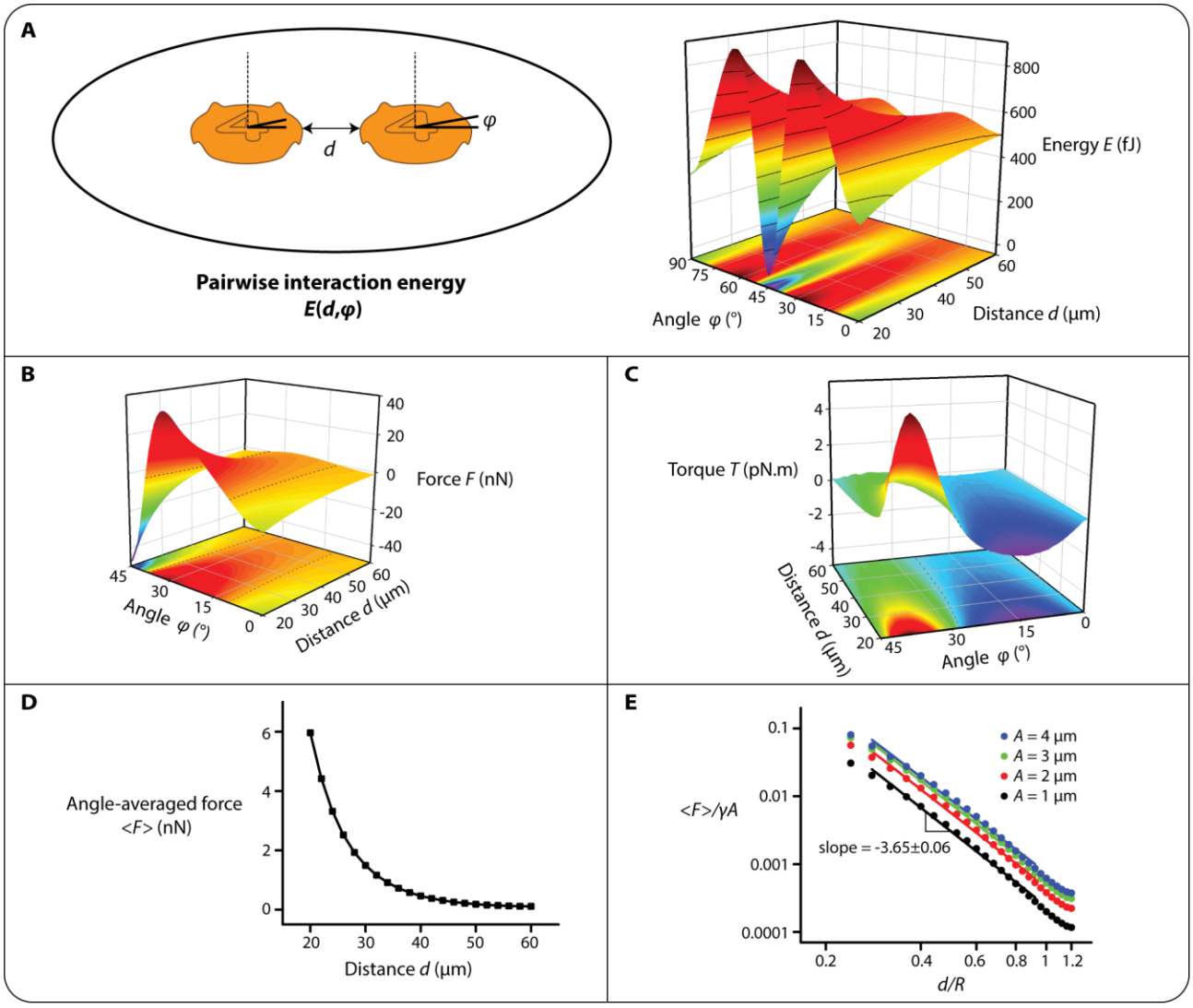

fig. S6. Preliminary quantitative studies of micro-raft pairwise interactions using the Surface Evolver program. (**A**) Schematic and 3D surface plot of the pairwise interaction energy E as a function of edge-to-edge distance d and micro-rafts' rotation angle φ. In Surface Evolver simulations, the energy was simulated per one degree rotation angle and per 2 μm distance. Because only relative value of energy is important, the zero point of the energy is selected to be the lowest energy value, which in this case is at d = 20 μm and φ = 45°. The energy plot is symmetric along φ = 45°, so subsequent force and torque plots are calculated only from 0° – 45°. The displayed 3D surface plots corresponds to micro-rafts with amplitude A = 4 μm and arc angle θ = 30°. (**B**) 3D surface plot of force F vs. d and φ, and its projection onto the bottom plane. Force is obtained through $F = -\partial E/\partial d$. Positive F denotes repulsion, and negative F denotes attraction. Repulsion is strongest at $\varphi \sim 30°$, where the nearest cosinusoidal profiles from two micro-rafts are misaligned. Attraction

is strongest at $\varphi = 45°$, where the cosinusoidal profiles from two micro-rafts are aligned. (**C**) 3D surface plot of torque T vs. d and φ, and its projection onto the bottom plane. Torque is calculated through $T = -\partial E/\partial\varphi$. Positive T denotes the tendency to increase φ, and negative T denotes the tendency to decrease φ. (**D**) Plot of angle-averaged force $\langle F \rangle$ vs. distance d. It is obtained from B by averaging the force over all angles. (**E**) log-log plot of force vs. distance to extract power law relation. The angle-averaged force $\langle F \rangle$ is divided by the product of the capillary tension $\gamma = 74$ mN/m and the amplitude of the cosinusoidal profile $A = 1 – 4$ μm. The distance d is divided by the radius of the raft $R = 50$ μm.

Note 1: The simulations in Surface Evolver provide equilibrium energy profile, and we use it to gain some insights into the first-order effect of capillary repulsion at the near field. Qualitatively, the angle-averaged force is repulsive in the near field, which agrees with what we observe experimentally. We are aware that this estimation is based on equilibrium calculation and that true energy profile in our non-equilibrium systems should be different. However, for a first-order estimation, the results are justified on the ground that the shape of the air-water interface should reach equilibrium shape within a few microseconds. It is much shorter than the period of a typical rotation, which is on the order of a few milliseconds. The estimation is below.

The group velocity of capillary waves $v_g \sim 3/2*(2\pi\gamma/\rho\lambda)^{1/2} \sim 3$ m/s, where $\gamma = 74$ mN/m is the surface tension of water, $\rho = 10^3$ kg/m^3 is the density of water, $\lambda = 100$ μm is the wavelength of the capillary wave. A typical distance between micro-rafts is 50 μm, so a typical time scale for the capillary wave to establish between micro-rafts is ~ 15 μs. As a comparison, the rotation speed of micro-rafts is up to 2500 rpm or 41.7 Hz, which corresponds to roughly a period of 24 ms.

Note 2: The doubly logarithmic plots in panel E indicate that the scaling relation of net repulsive force $\langle F \rangle$ vs. distance d is non-linear. In the region where experimental values of d fall, the net repulsive force $\langle F \rangle$ roughly scales with the inverse of the distance d to the power of 3 – 4. In addition, because $\langle F \rangle$ is an average over all angles, it sums both the repulsive and attractive forces. As a result, the magnitude of $\langle F \rangle$ is about two to three orders of magnitude less than the peak repulsive force at $\varphi \sim 30°$. At $d = 50$ μm, it is about 0.01 – 0.1 nN, which is comparable with the magnitudes of three other forces in the system, namely, the attractive magnetic force due to the confining potential of the permanent magnet, magnetic dipole-dipole interactions, and the hydrodynamic repulsive interactions at high spin speed (see fig. S1). A complete model may require the inclusion of all these forces to explain all the features of pairwise interactions. Nevertheless, capturing the behavior of micro-rafts assembling below a threshold Ω, such as shown in fig. S5, only requires capillary torque and force, and the overall magnetic potential, as illustrated below.

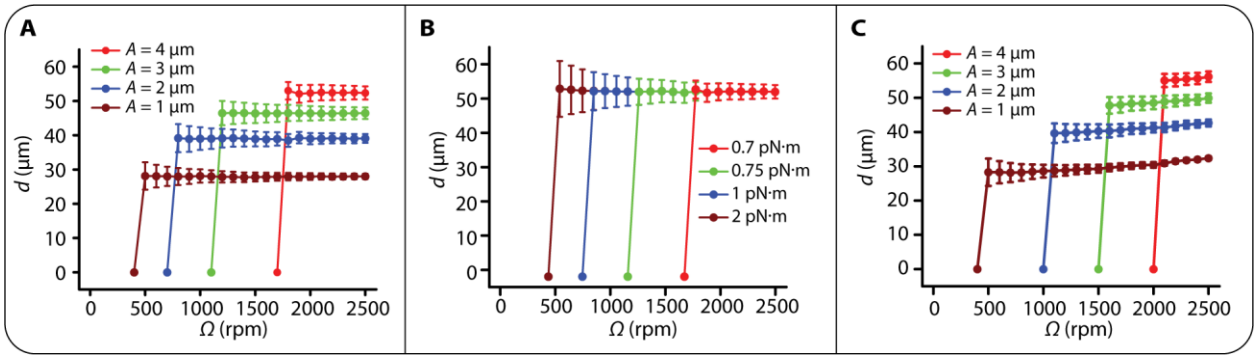

fig. S7. Simulated pairwise interaction curves. (**A**) Curves for different amplitudes with maximum magnetic torque 0.7 pN·m. (**B**) Curves for different maximum magnetic torque with A = 4 µm. The equation set in note 1 below is used for (A) and (B). (**C**) Repulsive hydrodynamic force is added in the simulation. It produces a decrease in distance as the spin speed Ω is lowered. See note 2 below.

Note 1: The curves in (A) and (B) are simulated based on the following equations:

$$\frac{d\boldsymbol{r_i}}{dt} = \frac{R^3\boldsymbol{\omega} \times (\boldsymbol{r_i} - \boldsymbol{r_j})}{|\boldsymbol{r_i} - \boldsymbol{r_j}|^3} + (6\pi\mu R)^{-1}\left(c_m m \frac{d^2 B_x}{dx^2}\boldsymbol{r_i} + c_c F_{cap}(A,d,\varphi)\frac{\boldsymbol{r_i} - \boldsymbol{r_j}}{|\boldsymbol{r_i} - \boldsymbol{r_j}|}\right), i,j = 1{,}2 \; or \; 2{,}1$$

$$\frac{d\alpha_i}{dt} = \omega = \Omega, \left(\tau_{mag,max} \geq \mathrm{T_{cap}}(A,d,\varphi)\right), i = 1{,}2$$

$$\frac{d\alpha_i}{dt} = -\frac{\mathrm{T}_{cap}(A,d,\varphi)}{6\pi\mu R^3}, \left(\tau_{mag,max} < \mathrm{T_{cap}}(A,d,\varphi)\right), i = 1{,}2$$

$\boldsymbol{r_i}$: Position vector of micro-raft i

$R = 50\ \mu m$: Radius of a micro-raft

$\omega = 100 - 2500\ rpm = 10.5 - \ 262\ rad/s$: Angular velocity of a micro-raft

$\mu = 1.0\ mPa \cdot s$: Dynamic viscosity of water

c_m: Constant of proportionality for magnetic force.

$m = 1.6 \times 10^{-10} A\ m^2$: Magnetic moment of one micro-raft, estimated from fig. S2

$\frac{d^2 B_x}{dx^2} = -2.15 \times 10^3 T/m^2$: Slope estimated in the plot dB_x/dx vs. x in fig. S3

c_c: Constant of proportionality for capillary force.

$F_{cap}(A, d, \varphi)$: Capillary force as a function of amplitude, distance between micro-rafts, and rafts' relative orientation angle. It is obtained from surface evolver simulation, as illustrated in fig. S6.

α_i: Rotation angle of micro-raft *i*. Note that this angle is different from rafts' relative orientation angle φ, because the micro-rafts are processing at the same as they are rotating.

$\tau_{mag,\max}$: Maximum magnetic torque. The value obtained from experimental measurement is $|\mathbf{m}\cdot\mathbf{B}|$ = 2 pN·m. Simulations suggest that this value is large but is in the correct of order of magnitude.

$T_{cap}(A, d, \varphi)$: Capillary torque as a function of amplitude, distance between micro-rafts, and rafts' relative orientation angle. It is obtained from surface evolver simulation, as illustrated in fig. S6.

After experimental values are inserted and position vectors are non-dimensionalized by *R*, the following equations are used in the simulation.

$$\frac{d\tilde{\boldsymbol{r}}_i}{d\tilde{t}} = \frac{\boldsymbol{\omega}\times\left(\tilde{\boldsymbol{r}}_i-\tilde{\boldsymbol{r}}_j\right)}{\left|\tilde{\boldsymbol{r}}_i-\tilde{\boldsymbol{r}}_j\right|^3} - 0.365s^{-1}c_m\tilde{\boldsymbol{r}}_i + \frac{c_c}{4.71\times10^{-2}nN\cdot s}F_{cap}(A,d,\varphi)\frac{\tilde{\boldsymbol{r}}_i-\tilde{\boldsymbol{r}}_j}{\left|\tilde{\boldsymbol{r}}_i-\tilde{\boldsymbol{r}}_j\right|}, i,j = 1,2\ or\ 2,1$$

In the simulation, c_m = 9 and c_c = 1 are used, and time step is 100 μs.

Note 2: In (C), the hydrodynamic repulsion is added to the position equation.

$$\frac{d\boldsymbol{r}_i}{dt} = \frac{R^3\boldsymbol{\omega}\times\left(\boldsymbol{r}_i-\boldsymbol{r}_j\right)}{\left|\boldsymbol{r}_i-\boldsymbol{r}_j\right|^3} + (6\pi\mu R)^{-1}\left(c_m m\frac{d^2B_x}{dx^2}\boldsymbol{r}_i + c_cF_{cap}(A,d,\varphi)\frac{\boldsymbol{r}_i-\boldsymbol{r}_j}{\left|\boldsymbol{r}_i-\boldsymbol{r}_j\right|} + c_h\rho\omega^2R^7\frac{\boldsymbol{r}_i-\boldsymbol{r}_j}{\left|\boldsymbol{r}_i-\boldsymbol{r}_j\right|^4}\right),$$
$$i,j = 1,2\ or\ 2,1$$

ρ: density of water, 10^3 kg/m^3.

c_h: constant of proportionality for hydrodynamic force.

After experimental values are inserted and position vectors are non-dimensionalized by *R*, the following equations are used in the simulation

$$\frac{d\tilde{\boldsymbol{r}}_i}{d\tilde{t}} = \frac{\boldsymbol{\omega}\times\left(\tilde{\boldsymbol{r}}_i-\tilde{\boldsymbol{r}}_j\right)}{\left|\tilde{\boldsymbol{r}}_i-\tilde{\boldsymbol{r}}_j\right|^3} - 0.365s^{-1}c_m\tilde{\boldsymbol{r}}_i + \frac{c_c}{4.71\times10^{-2}nN\cdot s}F_{cap}(A,d,\varphi)\frac{\tilde{\boldsymbol{r}}_i-\tilde{\boldsymbol{r}}_j}{\left|\tilde{\boldsymbol{r}}_i-\tilde{\boldsymbol{r}}_j\right|} +$$
$$1.33\times10^{-4}s\cdot c_h\cdot\omega^2\frac{\tilde{\boldsymbol{r}}_i-\tilde{\boldsymbol{r}}_j}{\left|\tilde{\boldsymbol{r}}_i-\tilde{\boldsymbol{r}}_j\right|^4}, \qquad i,j = 1,2\ or\ 2,1$$

In the simulation, c_m = 9, c_c = 1, and c_h = 4 are used, and time step is 100 μs.

The comparison between (A) and (C) indicate that the capillary repulsion is the dominant repulsion in our model system, whereas the hydrodynamic repulsion is of secondary importance.

Note 3: The assumption of low Reynolds number is assumed. The following calculation shows that Re < 1, and thus validates the assumption:

$$\mathrm{Re} = \frac{\omega R^2}{\nu} = \frac{(10.5\sim262)\times(5\times10^{-5})^2}{10^{-6}} = 0.026\sim0.65 < 1$$

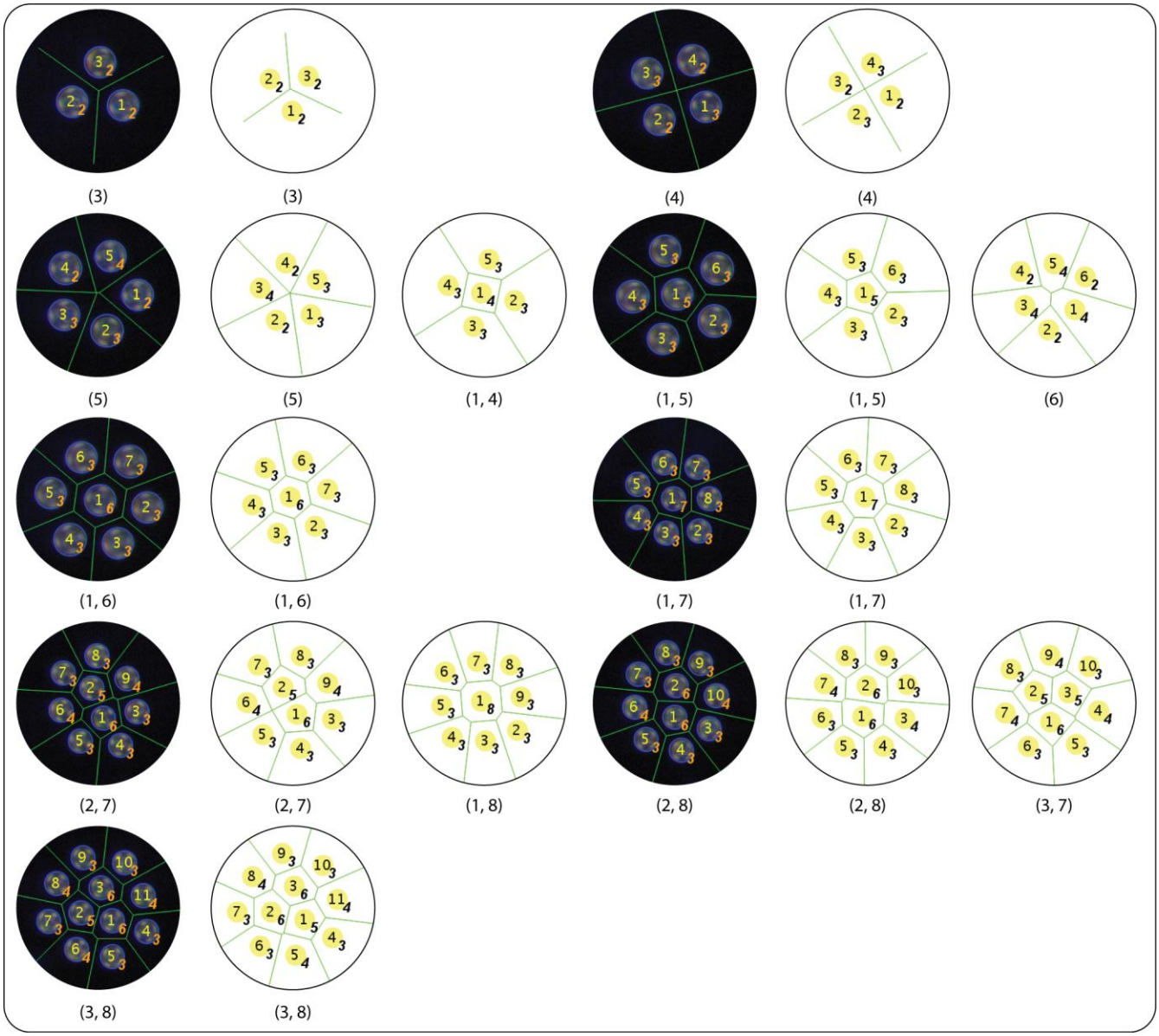

fig. S8. Experimental and simulated dynamic patterns for 3 to 40 micro-rafts. The number in parenthesis below each pattern indicates the number of micro-rafts in each layer. The first column of the simulated pattern corresponds to the experimental patterns. The rest patterns on its right side, if exist, are its polymorphs. Inside each pattern, the number at the center of a micro-raft is the micro-raft number. The micro-raft number starts from the innermost layer and increases clockwise within one layer. The number in italics at the bottom right of each micro-raft indicates the number of its nearest neighbors. This analysis of nearest neighbor is based on Voronoi cell construction.

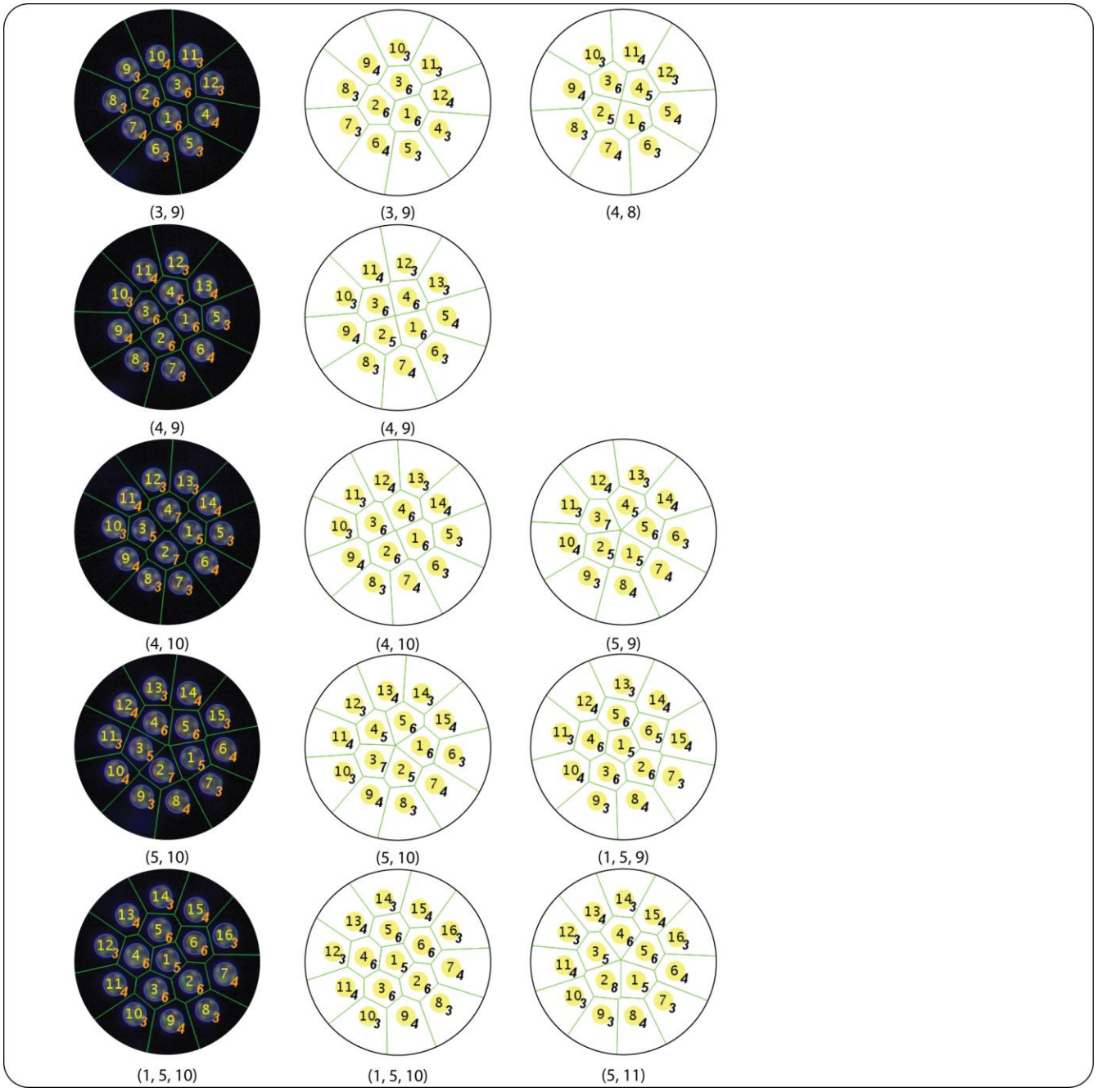

fig. S8. cont.

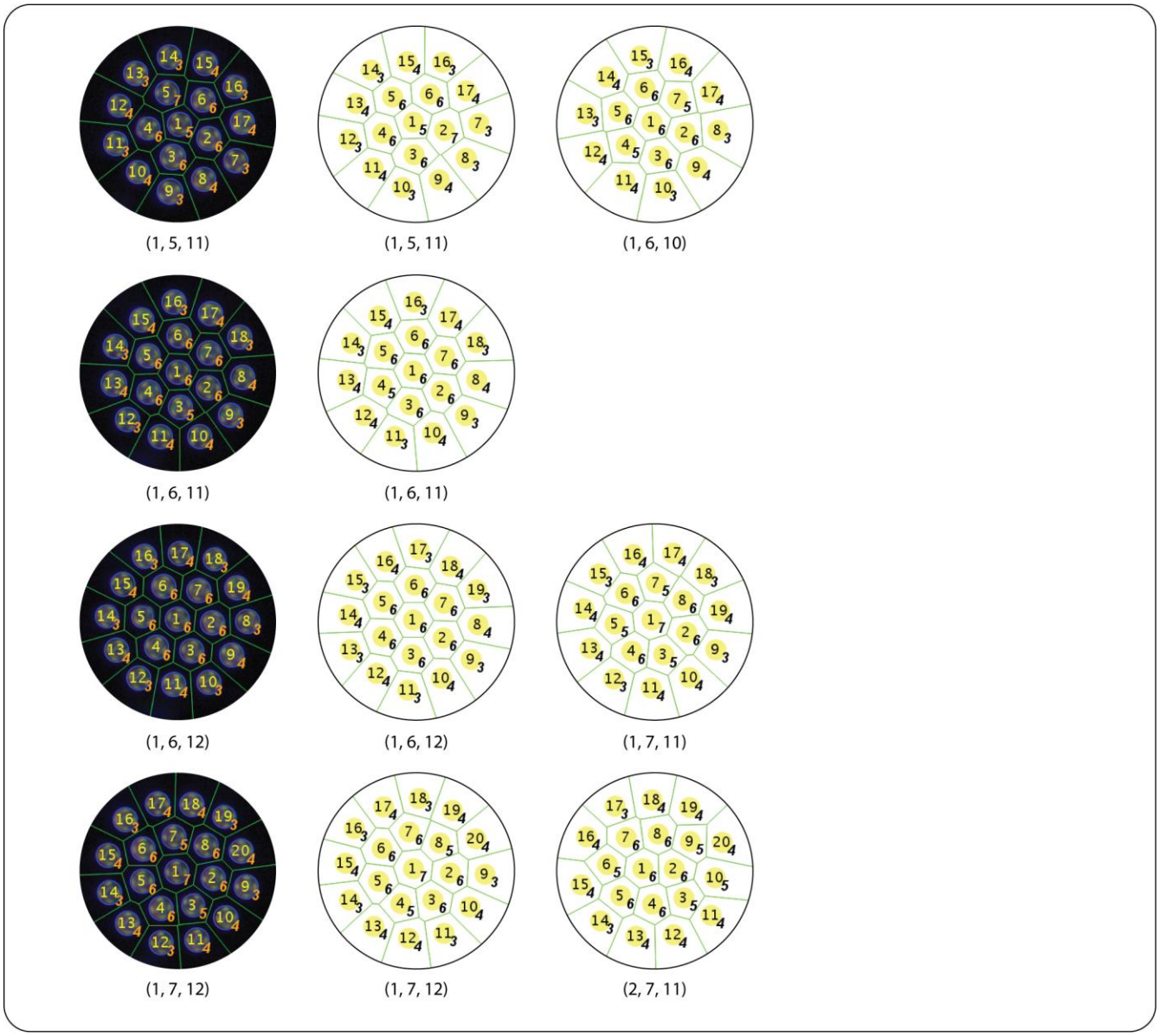

fig. S8. cont.

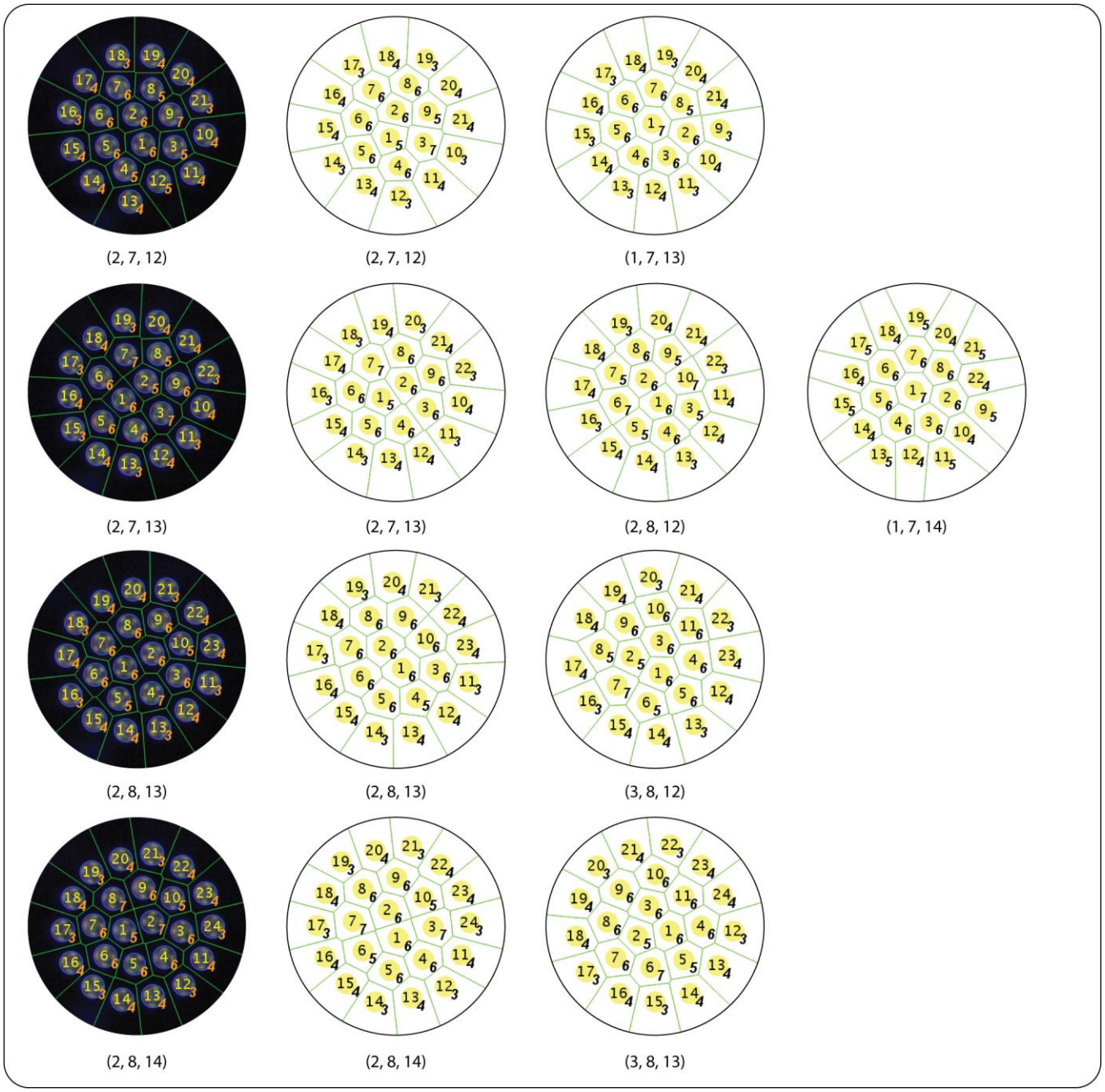
(2, 7, 12)
(2, 7, 12)
(1, 7, 13)
(2, 7, 13)
(2, 7, 13)
(2, 8, 12)
(1, 7, 14)
(2, 8, 13)
(2, 8, 13)
(3, 8, 12)
(2, 8, 14)
(2, 8, 14)
(3, 8, 13)

fig. S8. cont.

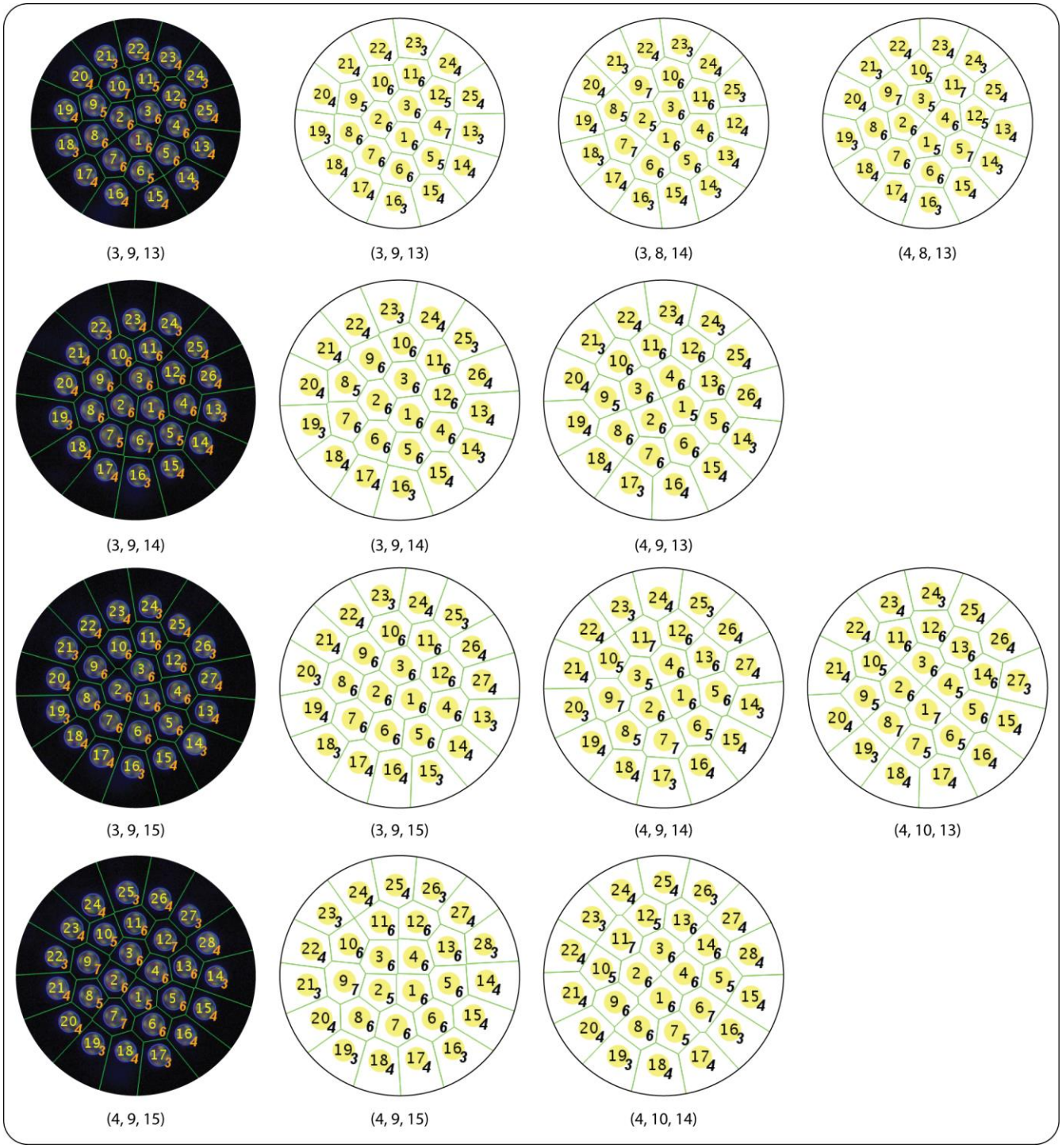
(3, 9, 13)
(3, 9, 13)
(3, 8, 14)
(4, 8, 13)
(3, 9, 14)
(3, 9, 14)
(4, 9, 13)
(3, 9, 15)
(3, 9, 15)
(4, 9, 14)
(4, 10, 13)
(4, 9, 15)
(4, 9, 15)
(4, 10, 14)

fig. S8. cont.

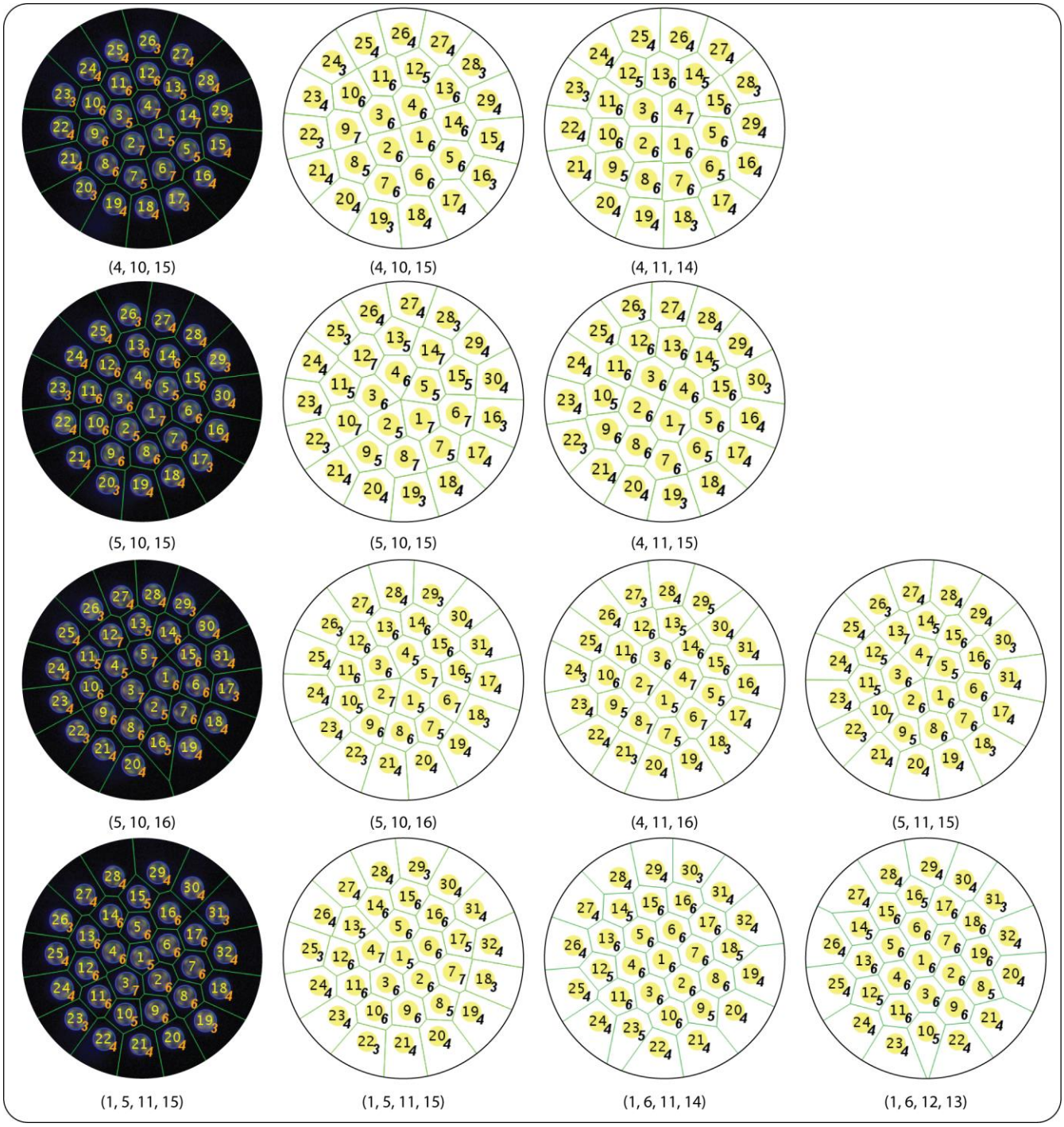
(4, 10, 15)
(4, 10, 15)
(4, 11, 14)
(5, 10, 15)
(5, 10, 15)
(4, 11, 15)
(5, 10, 16)
(5, 10, 16)
(4, 11, 16)
(5, 11, 15)
(1, 5, 11, 15)
(1, 5, 11, 15)
(1, 6, 11, 14)
(1, 6, 12, 13)

fig. S8. cont.

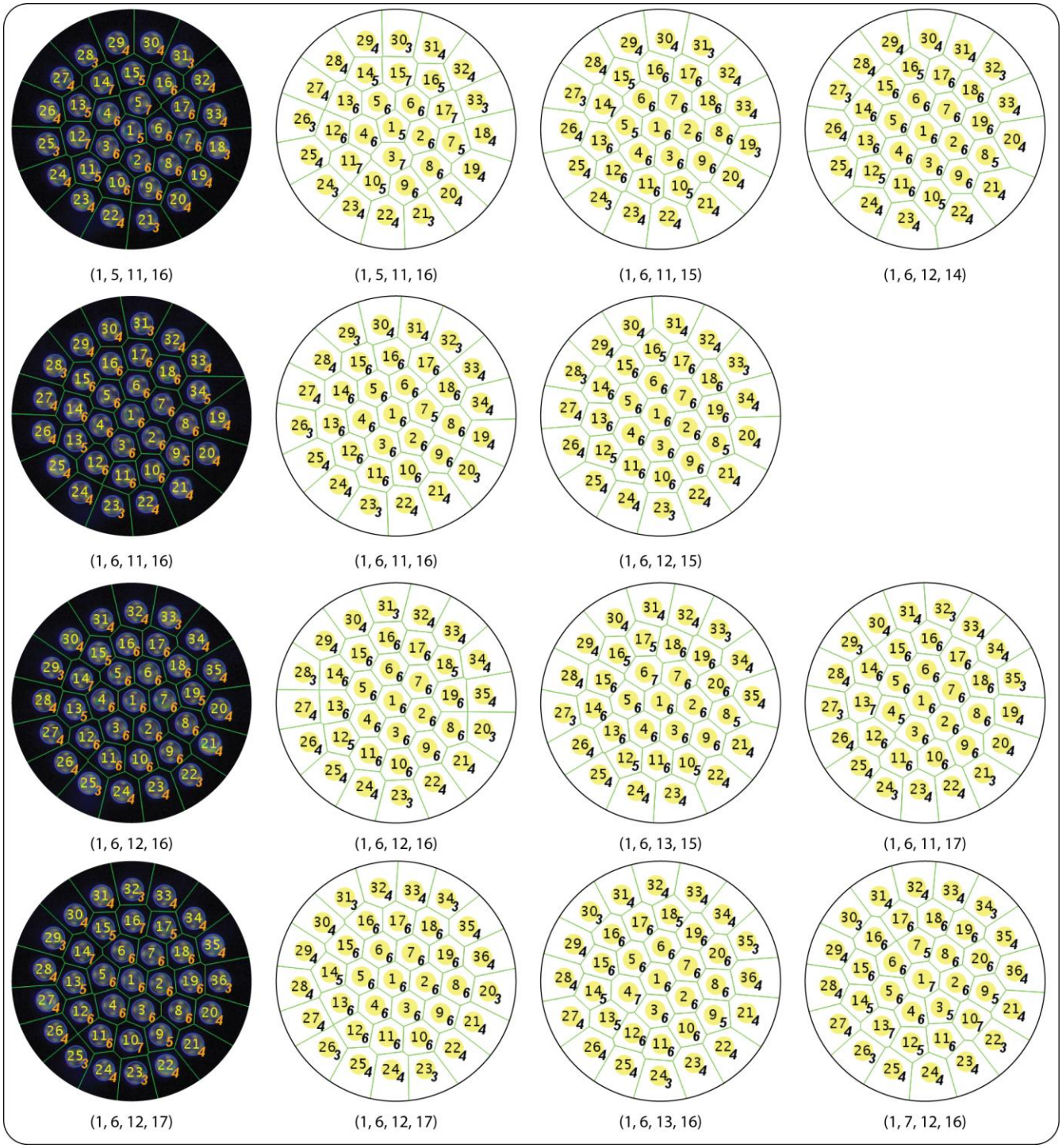
(1, 5, 11, 16)
(1, 5, 11, 16)
(1, 6, 11, 15)
(1, 6, 12, 14)
(1, 6, 11, 16)
(1, 6, 11, 16)
(1, 6, 12, 15)
(1, 6, 12, 16)
(1, 6, 12, 16)
(1, 6, 13, 15)
(1, 6, 11, 17)
(1, 6, 12, 17)
(1, 6, 12, 17)
(1, 6, 13, 16)
(1, 7, 12, 16)

fig. S8. cont.

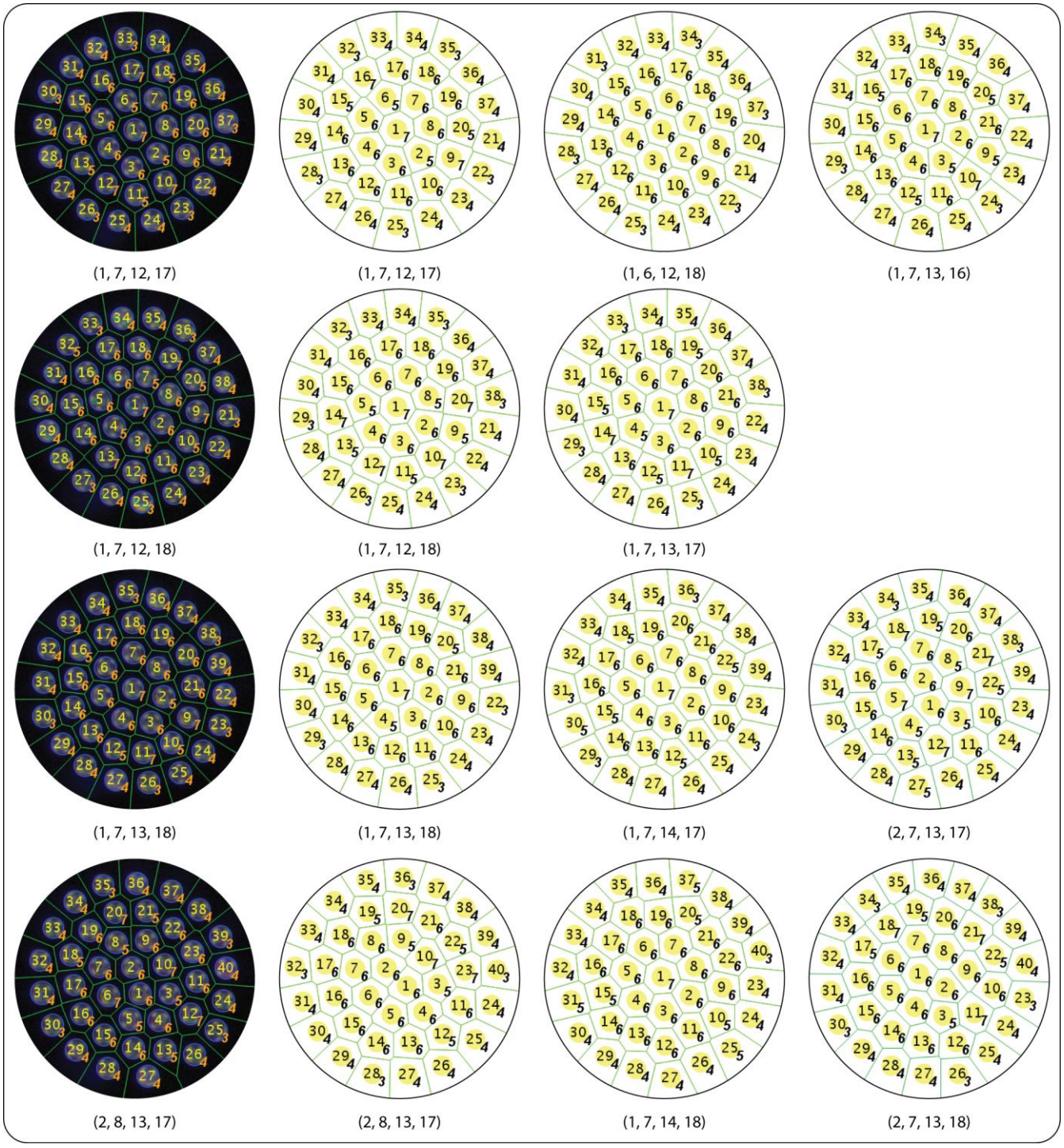
(1, 7, 12, 17)
(1, 7, 12, 17)
(1, 6, 12, 18)
(1, 7, 13, 16)
(1, 7, 12, 18)
(1, 7, 12, 18)
(1, 7, 13, 17)
(1, 7, 13, 18)
(1, 7, 13, 18)
(1, 7, 14, 17)
(2, 7, 13, 17)
(2, 8, 13, 17)
(2, 8, 13, 17)
(1, 7, 14, 18)
(2, 7, 13, 18)

fig. S8. cont.

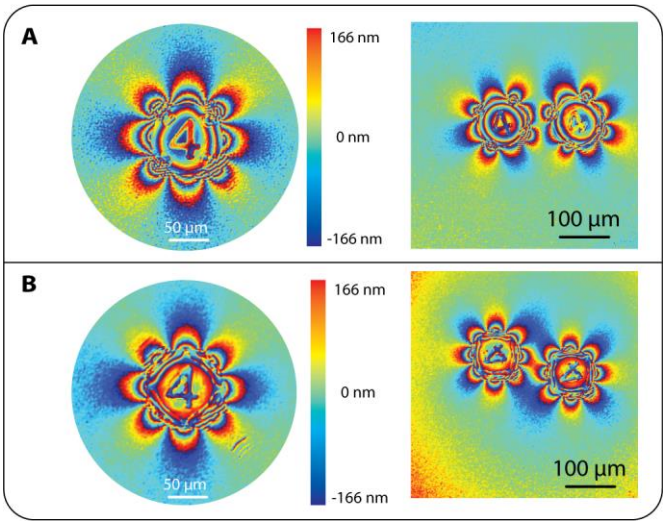

fig. S9. Comparison between the digital holographical micrographs of micro-rafts with arc angles of 30° and 90°. Comparison of digital holographical micrographs of micro-rafts with (**A**) arc angle θ = 30° and (**B**) arc angle θ = 90°. The four cosinusoidal profiles with arc angle θ = 30° are spaced apart by a flat region of arc angle 60°, and the interference pattern shows a 4-fold symmetry. The four cosinusoidal profiles with arc angle θ = 90° are connected with each other along the circumference of the micro-raft, and the interference pattern has $\bar{8}$-fold symmetry (8-fold rotary inversion symmetry, i.e. rotation by 45° and inversion through the center).

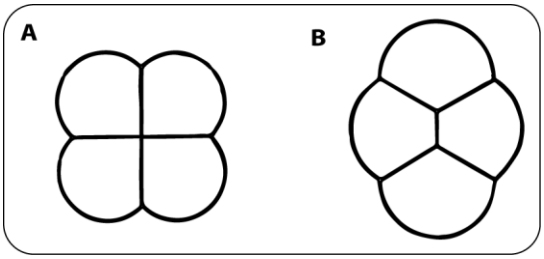

fig. S10. Unstable and stable configurations of aggregates of four bubbles. Retraced from Fig. 172, P486, Chapter VII of On Growth and Form, by D'Arcy Thompson, 1942, Cambridge [Eng.], The University Press. Original figure captions: (**A**) "an unstable arrangement of four cells or bubbles." (**B**) "the normal and stable configurations, showing the polar furrow."

Simulations

We modified the model in ref. 6 of the main text by changing the hydrodynamic repulsive interaction to capillary repulsive interaction.

$$\frac{d\boldsymbol{r_i}}{dt} = \sum_{j\neq i} \frac{R^3\boldsymbol{\omega}\times(\boldsymbol{r_i}-\boldsymbol{r_j})}{|\boldsymbol{r_i}-\boldsymbol{r_j}|^3} + (6\pi\mu R)^{-1}\left(c_m m\frac{d^2B_x}{dx^2}\boldsymbol{r_i} + c_c\gamma AR\theta\sum_{j\neq i}\frac{(\boldsymbol{r_i}-\boldsymbol{r_j})}{|\boldsymbol{r_i}-\boldsymbol{r_j}|}\frac{1}{|\boldsymbol{r_i}-\boldsymbol{r_j}|-2R}\right), i = 1, \dots N. \quad [1]$$

$\boldsymbol{r_i}$: Position vector of micro-raft *i*

$R = 50\ \mu m$: Radius of a micro-raft

$\omega = 2500\ rpm = 262\ rad/s$: Angular velocity of a micro-raft, which is the same as angular velocity of the spinning permanent magnet.

$\mu = 1.0\ mPa\ s$: Dynamic viscosity of water

c_m: Constant of proportionality for magnetic force

$m = 1.6\times10^{-10} A\ m^2$: Magnetic moment of one micro-raft, estimated from fig. S2

$\frac{d^2B_x}{dx^2} = -2.15\times10^3 T/m^2$: Slope estimated in the plot dB_x/dx vs. x in fig. S3

c_c: Constant of proportionality for capillary force

$\gamma = 74\ mN/m$: Surface tension of water

$A = 2\ \mu m$: Amplitude of a cosinusoidal curve

$\theta = \pi/6$: Arc angle of a cosinusoidal curve

The equation can be casted in non-dimensional form:

$$\frac{d\tilde{\boldsymbol{r}}_{\boldsymbol{i}}}{d\tilde{t}} = \sum_{j\neq i}\frac{\hat{z}\times(\tilde{\boldsymbol{r}}_{\boldsymbol{i}}-\tilde{\boldsymbol{r}}_{\boldsymbol{j}})}{|\tilde{\boldsymbol{r}}_{\boldsymbol{i}}-\tilde{\boldsymbol{r}}_{\boldsymbol{j}}|^3} + C_m\tilde{r}_i + C_c\sum_{j\neq i}\frac{(\tilde{\boldsymbol{r}}_{\boldsymbol{i}}-\tilde{\boldsymbol{r}}_{\boldsymbol{j}})}{|\tilde{\boldsymbol{r}}_{\boldsymbol{i}}-\tilde{\boldsymbol{r}}_{\boldsymbol{j}}|}\frac{1}{|\tilde{\boldsymbol{r}}_{\boldsymbol{i}}-\tilde{\boldsymbol{r}}_{\boldsymbol{j}}|-2}, i = 1, \dots N \qquad [2]$$

with $\tilde{\boldsymbol{r}}_{\boldsymbol{i}} = \boldsymbol{r_i}/R$, $\tilde{t} = t\omega$, $C_m = \frac{c_m m\frac{dB_x}{dx^2}}{6\pi\mu R\omega} = -1.39\times10^{-3}c_m$, $C_c = \frac{c_c\gamma A\theta}{6\pi\mu R^2\omega} = 6.28c_c$.

Determine parameters C_m and C_c:

Following the procedure outlined in ref. 6 of the main text, we use data from pairwise interaction to determine c_m and c_c. From fig. S5A, we obtain edge-to-edge distance $d = 64\ \mu m$ at $\omega = 2500\ rpm$, so $|\boldsymbol{r_1}| = |\boldsymbol{r_2}| = 1 + \frac{1}{2}\frac{64}{50} = 1.64$. Furthermore, by equating magnetic term and capillary term, we obtain

$c_c/c_m = 4.6\times10^{-4}$, and by adjusting of value of c_m to meet the experimental value of d, we obtain $c_m = 120$, and $c_c = 5.52\times10^{-2}$. Consequently, $C_m = -0.1668, C_c = 0.3468$.

Numerical integrations of equations [2] were iterated 10,000 – 100,000 steps to reach stable configuration.

Notes on other forms of scaling laws of repulsive capillary forces:

We also tried simulations with the following two equations:

$$\frac{d\tilde{\boldsymbol{r}}_{\boldsymbol{i}}}{d\tilde{t}} = \sum_{j\neq i} \frac{\hat{z}\times\left(\tilde{\boldsymbol{r}}_{\boldsymbol{i}}-\tilde{\boldsymbol{r}}_{\boldsymbol{j}}\right)}{\left|\tilde{\boldsymbol{r}}_{\boldsymbol{i}}-\tilde{\boldsymbol{r}}_{\boldsymbol{j}}\right|^{3}} + C_m\tilde{r}_i + C_c\sum_{j\neq i}\frac{\left(\tilde{\boldsymbol{r}}_{\boldsymbol{i}}-\tilde{\boldsymbol{r}}_{\boldsymbol{j}}\right)}{\left|\tilde{\boldsymbol{r}}_{\boldsymbol{i}}-\tilde{\boldsymbol{r}}_{\boldsymbol{j}}\right|}\frac{1}{\left(\left|\tilde{\boldsymbol{r}}_{\boldsymbol{i}}-\tilde{\boldsymbol{r}}_{\boldsymbol{j}}\right|-2\right)^{3}}, i=1,\dots N \qquad [3]$$

$$\frac{d\tilde{\boldsymbol{r}}_{\boldsymbol{i}}}{d\tilde{t}} = \sum_{j\neq i} \frac{\hat{z}\times\left(\tilde{\boldsymbol{r}}_{\boldsymbol{i}}-\tilde{\boldsymbol{r}}_{\boldsymbol{j}}\right)}{\left|\tilde{\boldsymbol{r}}_{\boldsymbol{i}}-\tilde{\boldsymbol{r}}_{\boldsymbol{j}}\right|^{3}} + C_m\tilde{r}_i + C_c\sum_{j\neq i}\frac{\left(\tilde{\boldsymbol{r}}_{\boldsymbol{i}}-\tilde{\boldsymbol{r}}_{\boldsymbol{j}}\right)}{\left|\tilde{\boldsymbol{r}}_{\boldsymbol{i}}-\tilde{\boldsymbol{r}}_{\boldsymbol{j}}\right|}\frac{1}{\left(\left|\tilde{\boldsymbol{r}}_{\boldsymbol{i}}-\tilde{\boldsymbol{r}}_{\boldsymbol{j}}\right|-2\right)^{4}}, i=1,\dots N\ , \qquad [4]$$

in which the repulsive capillary forces scale with ~1/d^3 or ~1/d^4. The results are essentially similar in the way that the micro-rafts are "close-packed" by the confining potential. It suggests that the detail of how the capillary repulsive force decays over distance may not be essential in producing patterns of dynamic self-assembly.

Description of supporting videos:

movie S1. Examples of pairwise interactions.

movie S2. Two polymorphs of the dynamic patterns formed by 21 micro-rafts.

movie S3. Four examples of nearest-neighbor counts in dynamically self-assembled patterns.

movie S4. The assembly of three free micro-rafts with an arc angle of 30°.

movie S5. The assembly of one free and two attached micro-rafts with an arc angle of 30°.

movie S6. The assembly of four free micro-rafts with an arc angle of 30°.

movie S7. The assembly of one free and three attached micro-rafts with an arc angle of 30°.

movie S8. The assembly of four free micro-rafts with an arc angle of 90°.

movie S9. The disassembly of four assembled micro-rafts with an arc angle of 90°.

movie S10. The rearrangement of four assembled micro-rafts with an arc angle of 90° into a diamond shape.

movie S11. The rearrangement of four assembled micro-rafts with an arc angle of 90° into a square shape.

movie S12. The assembly of 40 micro-rafts with an arc angle of 30°.

movie S13. The assembly of 40 micro-rafts with an arc angle of 90°.

movie S14. The local rearrangement of assembled structures of 40 micro-rafts with an arc angle of 30° at intermediate spinning speed.